

DISK WINDS DRIVEN BY MAGNETOROTATIONAL INSTABILITY AND DISPERSAL OF PROTO-PLANETARY DISKS

TAKERU K. SUZUKI¹ & SHU-ICHIRO INUTSUKA²*Submitted to ApJ*

ABSTRACT

By performing local three-dimensional MHD simulations of stratified accretion disks, we investigate disk winds driven by MHD turbulence. Initially weak vertical magnetic fields are effectively amplified by magnetorotational instability and winding due to differential rotation. Large-scale channel flows develop most effectively at 1.5 - 2 times the scale heights where the magnetic pressure is comparable to but slightly smaller than the gas pressure. The breakup of these channel flows drives structured disk winds by transporting the Poynting flux to the gas. These features are universally observed in the simulations of various initial fields. This disk wind process should play an essential role in the dynamical evaporation of protoplanetary disks. The breakup of channel flows also excites the momentum fluxes associated with Alfvénic and (magneto-)sonic waves toward the midplane, which possibly contribute to the sedimentation of small dust grains in protoplanetary disks.

Subject headings: accretion, accretion disks — ISM: jets and outflows — MHD — planetary systems: protoplanetary disks — planetary systems: formation — turbulence

1. INTRODUCTION

Magnetorotational instability (MRI; Balbus & Hawley 1991) is regarded as a robust mechanism to provide turbulence for an efficient outward transport of angular momentum in accretion disks. MHD simulations in a local shearing box have been carried out (e.g., Hawley, Gammie, & Balbus 1995; Brandenburg et al. 1995; Sano et al. 2004) to study the properties of MRI-driven turbulence. Miller & Stone (2000) studied vertically stratified local disks with free boundaries to allow leaks of mass and magnetic field. While their main purpose is to study general properties of stratified disks such as disk coronae rather than disk winds, they concluded that the mass flux of the outflows is small in the cases of initially toroidal and zero-net vertical flux magnetic fields.

On the other hand, protoplanetary disks around young stars should have net vertical magnetic fields that are connected to their parental molecular clouds. In this case, the physical conditions of the surface of the disk are analogous to the open coronal holes of the Sun where the solar wind is driven by turbulent footpoint motions of the magnetic field lines (Sakao et al. 2007; Tsuneta et al. 2008). Obviously, MHD turbulence excited by MRI in the disk is also expected to drive winds from the surfaces of the accretion disk. Although such a disk wind mechanism may play a significant role in the evolution of accretion disks (Ferreira, Dougados & Cabrit 2006), quantitative studies have not been carried out so far because of difficulties in the numerical treatment: a long-term calculation of the wind process requires accurate description of outgoing boundary conditions for various types of waves, rather than simple free boundaries³.

Electronic address: stakeru@ea.c.u-tokyo.ac.jp

¹ School of Arts and Sciences, University of Tokyo, Komaba, Meguro, Tokyo, Japan, 153-8902

² Department of Physics, Kyoto University, Kyoto, Japan, 606-8502

³ Simple free boundaries means setting the derivatives of variables to be zero. In this case, however, unphysical reflections of

In this Letter, we investigate disk winds driven by MRI with initially vertical magnetic fields utilizing the rigorous outgoing boundary condition that was originally developed for the simulations of solar (Suzuki & Inutsuka 2005, 2006) and stellar (Suzuki 2007) winds.

2. SETUP

We perform 3D MHD simulations in a local shearing box (Hawley et al. 1995), taking into account vertical stratification (Stone et al. 1996; Turner & Sano 2007). We set the x -, y -, and z -coordinates as the radial, azimuthal, and vertical directions, respectively. We solve the ideal MHD equations with an isothermal equation of state in a frame corotating with Kepler rotation. In the momentum equation we consider the vertical gravity by a central star, $\Omega_0^2 z$, where Ω_0 is Keplerian rotation frequency. We adopt a second-order Godunov-CMoCCT scheme, in which we solve nonlinear Riemann problems with magnetic pressure at cell boundaries for compressive waves and adopt the consistent method of characteristics (CMoC) for the evolution of magnetic fields (Clarke 1996).

The simulation region is $(x, y, z) = (\pm 0.5H_0, \pm 2H_0, \pm 4H_0)$, and is resolved by (32,64,256) grid points, where $H_0 = \sqrt{2}c_s/\Omega_0$ is the pressure scale height for sound speed, c_s . The shearing boundary is adopted for the x -direction to consider the Keplerian shear flow (Hawley et al. 1995). The simple periodic boundary is adopted for the y -direction. We prescribe the outflow condition in the z -directions by adopting only outgoing characteristics from all seven (six for isothermal gas) MHD characteristics at the $z = \pm 4H_0$ boundaries (Suzuki & Inutsuka 2006). While the z -component of the magnetic flux is strictly conserved, the x - and y -components are not conserved because of the outgoing condition at the z boundaries. We initially set

waves usually occur. For the real outgoing boundary, only the derivatives of incoming characteristics should vanish (Thompson 1987).

up a hydrostatic density structure, $\rho = \rho_0 \exp(-z^2/H_0^2)$, with $\rho_0 = 1$, and a constant vertical magnetic field, $B_{z,0}$, with the plasma β value, $\beta_0 = 8\pi\rho_0 c_s^2/B_{z,0}^2 = 10^6$ (for our fiducial model) at the midplane. We use $\Omega_0 = 1$ and $H_0 = 1$, which gives $c_s^2 = 1/2$. Small random perturbations, $\delta v = 0.005c_s$, are initially given for the seeds of MRI.

3. RESULTS

In most of the simulation region, the initial magnetic fields are moderately weak, so it is unstable with respect to MRI. In $|z| < 2.5H_0$, however, we cannot initially resolve the wavelengths, $\lambda_{\max} \approx 2\pi v_A/\Omega_0$, of the most unstable mode because $\lambda_{\max} < \Delta z (= H_0/32)$, where $v_A = B/\sqrt{4\pi\rho}$ is Alfvén speed and Δz is the mesh size (the initial $\lambda_{\max} \approx 0.2\Delta z$ at the midplane). First, MRI develops around $z \approx \pm 3H_0$ after ≈ 3 rotations. The turbulence driven by MRI gradually spreads toward the midplane, since the growth time (approximately $\propto \Delta z/\lambda_{\max}$ for $\Delta z > \lambda_{\max}$) of the resolved wavelength is longer there. When $t \gtrsim 100$ rotations, the midplane finally becomes turbulent. The magnetic field strength saturates in the entire box after $t \gtrsim 200$ rotations, and the system becomes quasi-steady-state. At this time, λ_{\max} can be resolved even at the midplane owing to the increase of the field strength. We continue the simulation further up to 400 rotations.

Figure 1 is the snapshot of magnetic field (white lines), velocity field (arrows), and $\delta\rho/\langle\rho\rangle$ (color) at $t = 210$ rotations, where $\langle\rho\rangle$ is the density averaging over each x - y plane and $\delta\rho = \rho - \langle\rho\rangle$. The magnetic fields are turbulent, dominated by the toroidal (y) component because of winding. Angular momentum is outwardly transported by anisotropic stress due to the MHD turbulence. At the saturated state, $\alpha \equiv (v_x \delta v_y - \frac{B_x B_y}{4\pi\rho})/c_s^2$ is ~ 0.01 in the midplane. One can also observe that the structured outflows stream out from both the upper and lower boundaries. Below we inspect the properties of the outflows in more detail.

Figure 2 presents the mass flux of the z -component, $\rho v_z/\rho_0 c_s$, in the $t - z$ plane. We averaged ρv_z on the x - y plane at each z grid point. One can see that the gas flows out from both the upper and lower boundaries. The mass fluxes near the surface regions are highly time dependent with a quasi-periodic cycle of $\sim 5 - 10$ rotations. Moreover, from $z \sim \pm 2H_0$ the mass fluxes direct to the midplane, almost coinciding with the periodicities of the outflow fluxes. In other words, the mass flows are ejected to both upward and downward directions from ‘injection regions’ located at $z \sim \pm 2H_0$.

These features are consequences of the breakup of channel flows (e.g., Sano & Inutsuka 2001; Sano et al. 2004). At $z \sim \pm 2H_0$, the wavelength of the most unstable mode with respect to MRI, λ_{\max} , is comparable with the scale height, H_0 . In the region $|z| > 2H_0$, $\lambda_{\max} > H_0$; hence, it is stable against MRI. In the region $|z| < 2H_0$, smaller-scale turbulence develops preferentially because $\lambda_{\max} < H_0$. Therefore, at $z \sim \pm 2H_0$ the largest scale channel flows develop, and their breakup by reconnections⁴ drives the mass flows to both upward and down-

⁴ We do not explicitly include the physical resistivity term in the calculation shown in this Letter, and so, the reconnections are due to the numerical effect determined by the grid scale.

ward directions. In the region $|z| < 2H_0$, the gas pressure largely dominates the magnetic pressure so that strong mass flows cannot be driven by the magnetic force associated with reconnections between small-scale turbulent fields. The periodic oscillation of 1 Keplerian rotation time around the midplane is the vertical (epicycle) motion.

Figure 3 presents the disk wind structure averaged over 200 - 400 rotations. The variables are averaged on the x - y plane at each z point. The top panel shows that the average outflow velocity is nearly the sound speed at the upper and lower surfaces. The second panel presents the structures of density and plasma β value. The comparison of the final density structure (solid) with the initial hydrostatic structure (dotted) shows that the mass is loaded up to the onset regions of outflows from $z \approx \pm 2H_0$. In the wind region $|z| \gtrsim 3H_0$, β is below unity; the disk winds start to accelerate when the magnetic pressure dominates the gas pressure.

The third panel shows magnetic energy at the saturated state. The dashed, solid, and dotted lines are x -, y -, and z -components, respectively. In the y -component we show both mean, $\langle B_y \rangle^2$ and fluctuation, δB_y^2 , components. $\langle B_y \rangle^2$ is the simple average on the x - y planes, $\langle B_y(z) \rangle = \int \int dx dy B_y(x, y, z) / (L_x L_y)$, and the fluctuations are determined from $\delta B_y^2(z) = \int \int dx dy (B_y(x, y, z) - \langle B_y(z) \rangle)^2 / (L_x L_y)$, where $L_x (= H_0)$ and $L_y (= 4H_0)$ are the x and y lengths of the simulation box. As for B_x and B_z the fluctuation components greatly dominate the means. The magnetic energy, which is dominated by the toroidal (y) component as a consequence of winding, is amplified by ≈ 1000 times of the initial value ($B_{z,0}^2/4\pi = 10^{-6}$) in most of the region ($|z| < 3H_0$). While in the region near the midplane ($|z| < 1.5H_0$), the magnetic field is dominated by the fluctuating component (δB_y), the mean component dominates in the regions near the surfaces ($|z| > 1.5H_0$). In the surface regions the magnetic pressure is comparable to or larger than the gas pressure ($\beta \lesssim 1$), and so, the gas motions cannot control the configuration of the magnetic fields. Therefore, the field lines tend to be straightened by magnetic tension to give $\langle B \rangle^2 > \delta B^2$ there, even if the gas is turbulent. We also note that $\langle B_z^2 \rangle$ is amplified by MRI and Parker (1966) instability, whereas $\langle B_z \rangle^2$ is strictly conserved.

The bottom panel shows the status of energy transfer. The z -component of the total energy flux is expressed as

$$\rho v_z \left(\frac{1}{2} v^2 + \Phi + h \right) + v_z \frac{B_\perp^2}{4\pi} - \frac{B_z}{4\pi} (v_\perp B_\perp), \quad (1)$$

where h is the enthalpy⁵, $\Phi = z^2/2$, and \perp denotes x and y ; e.g. $B_\perp^2 = B_x^2 + B_y^2$. The Poynting flux is separated from the term of direct transport of magnetic energy ($B_\perp^2 v_z/4\pi$) and the term related to magnetic tension ($-B_z v_\perp B_\perp/4\pi$). The solid and dotted lines are respectively $-B_z \delta v_\perp B_\perp/4\pi$ and $B_\perp^2 v_z/4\pi$, where $\delta v_\perp = v_x$ and $v_y + 3/2\Omega_0 x$ ($-3/2\Omega_0 x$ is the background Kepler rotation). The dashed line is the potential energy term, $\rho v_z \Phi$. The dot-dashed line is the energy flux of sound waves, $\delta\rho \delta v_z c_s^2$ (see below). The gas pressure (ρv_z) and hydrodynamical turbulent pressure ($\rho \delta v^2 v_z/2$) are smaller

⁵ Formally, $h = c_s^2 \log \rho$ for isothermal gas

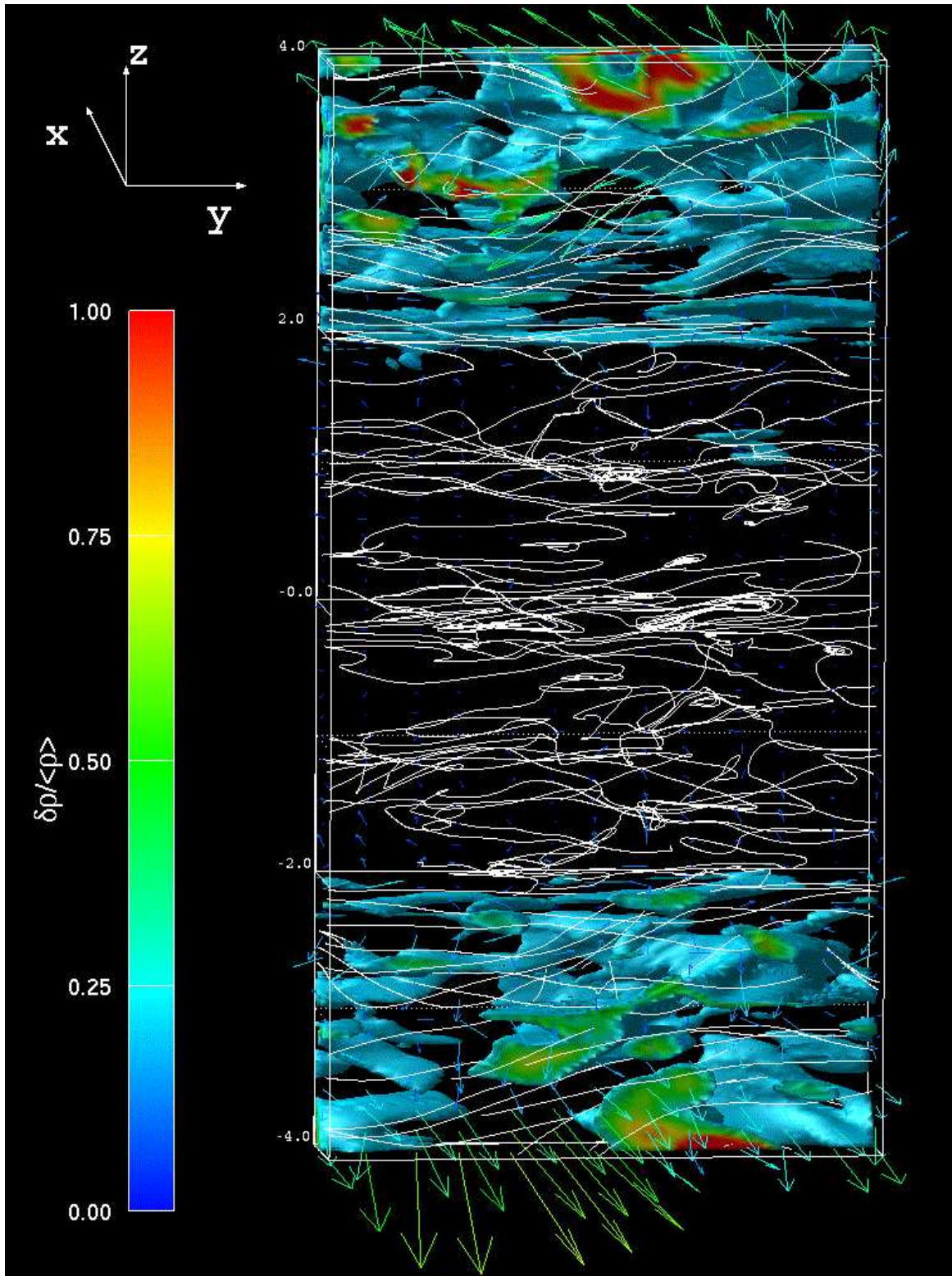


FIG. 1.— Snapshot of the local disk structure at $t = 210$ rotations. The white solid lines are magnetic fields, the arrows indicate velocity fields, and the colored region corresponds to $\delta\rho/\langle\rho\rangle > 0$.

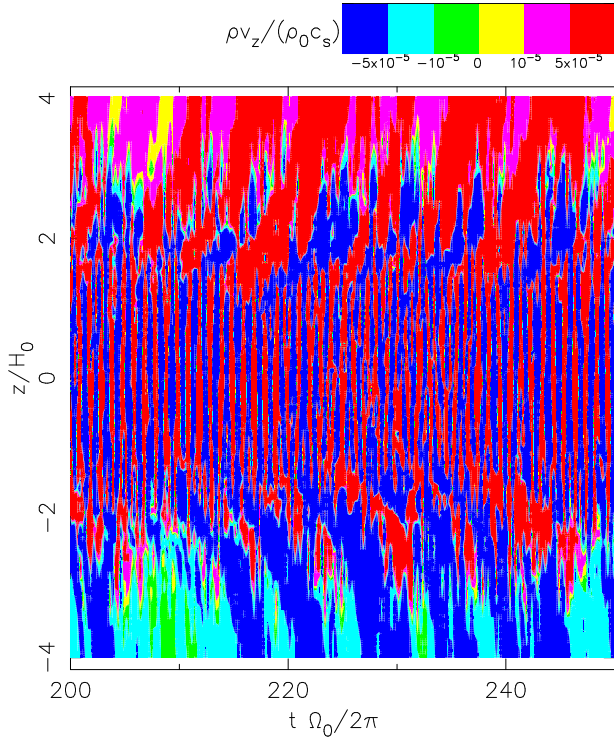


FIG. 2.— Time-height diagram of the mass flux, ρv_z , normalized by $\rho_0 c_s$. ρv_z is averaged on the x - y plane at each height, z (vertical axis). The unit of horizontal axis is the rotation period ($2\pi/\Omega_0$).

than these terms. The kinetic energy flux of the winds ($\frac{1}{2}\rho v_z^3$) is also small $\lesssim 10^{-5}$ at the outer boundaries.

The figure shows that the materials near the surfaces are lifted up by the conversion of the Poynting flux; the absolute values of the Poynting flux terms (solid and dotted) decrease with height in the region $|z| \gtrsim 2H_0$, and the absolute value of the potential energy flux (dashed) increases. Both magnetic pressure and tension terms contribute almost equally.

$-B_z \delta v_\perp B_\perp / 4\pi$ and $\delta \rho \delta v_z c_s^2$ are the net energy fluxes of Alfvén waves and sound waves to the $+z$ -direction. $-B_z \delta v_\perp B_\perp / 4\pi$ can be rewritten as

$$-\frac{1}{4\pi} B_z \delta v_\perp B_\perp = \rho v_{A,z} (\delta v_{\perp,+}^2 - \delta v_{\perp,-}^2), \quad (2)$$

where $v_{A,z} = B_z / \sqrt{4\pi\rho}$, and $\delta v_{\perp,\pm} = \frac{1}{2}(\delta v_\perp \mp B_\perp / \sqrt{4\pi\rho})$ are Elsässer variables, which correspond to the amplitudes of Alfvén waves propagating to the $\pm z$ -directions. $\delta \rho \delta v_z c_s^2$ is also rewritten as

$$\delta \rho \delta v_z c_s^2 = \rho c_s (\delta v_{\parallel,+}^2 - \delta v_{\parallel,-}^2), \quad (3)$$

where $\delta v_{\parallel,\pm} = \frac{1}{2}(\delta v_z \pm c_s \frac{\delta \rho}{\rho})$ denote the amplitudes of sound waves⁶ propagating in the $\pm z$ -directions.

An interesting feature of $-B_z \delta v_\perp B_\perp / 4\pi$ is that the sign changes at $z \approx \pm 1.6H_0$ (the circles in the bottom panel); in $z > 1.6H_0$ ($< -1.6H_0$), the flux is upward (downward) and $|z| < 1.6H_0$ the flux is toward

⁶ Strictly speaking, these are magnetosonic waves, namely the fast mode in the high β plasma, and the slow mode that propagates along z in the low β plasma. Note also that the signs are opposite for $\delta v_{\perp,\pm}$ and $\delta v_{\parallel,\pm}$, reflecting the transverse and longitudinal characters.

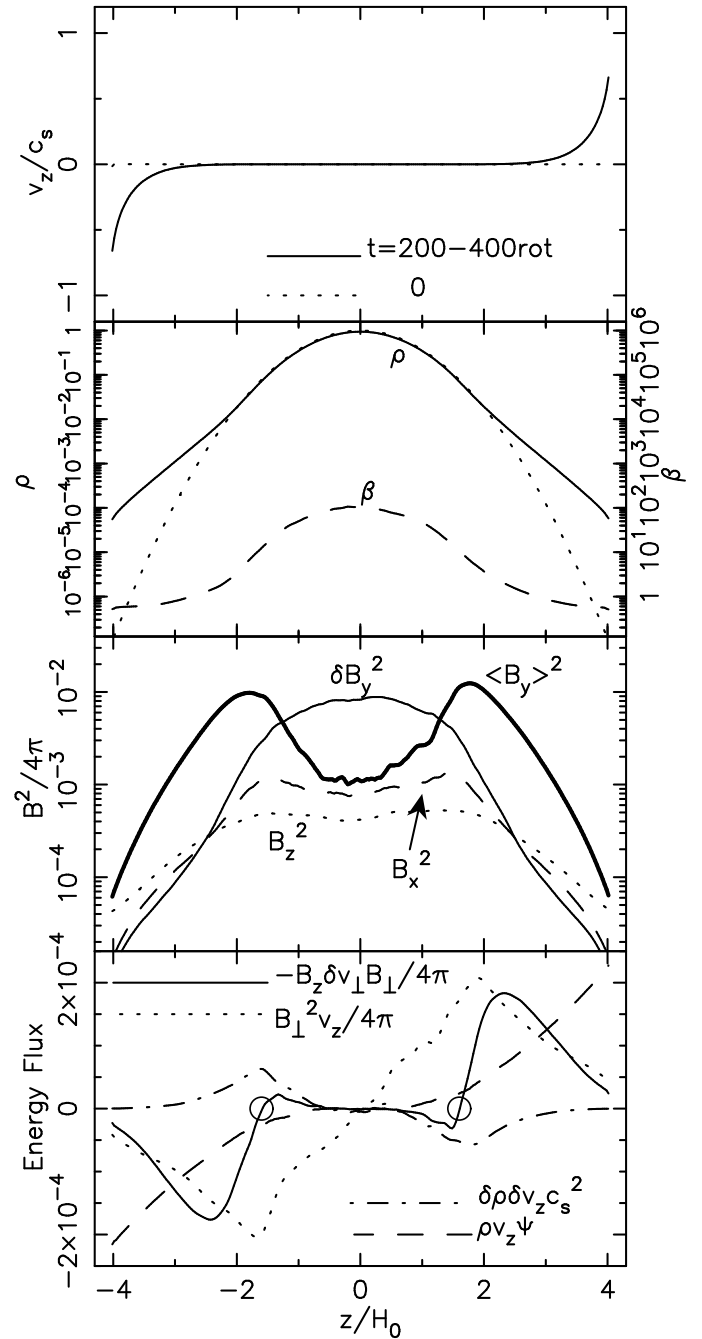


FIG. 3.— Time-averaged disk structure during $t = 200-400$ rotations. The variables are also averaged on the x - y plane at each z grid. The top panel shows v_z/c_s (solid), whereas the dotted line is the initial condition ($v_z/c_s = 0$). The second panel presents density (solid; left axis) and plasma β (dashed; right axis), in comparison with the initial condition (dotted; for both density and plasma β). The third panel presents the magnetic energy, $B^2/4\pi$. The dashed, solid, and dotted lines correspond to the x -, y -, and z -components, and the y -component shows both mean (thick) and fluctuation (thin) components. The bottom panel illustrates the energy flux in units of $\rho_0 (H_0 \Omega)^3$. The solid and dotted lines are the Poynting flux associated with the magnetic tension ($-B_z \delta v_\perp B_\perp / 4\pi$) and the magnetic energy ($B_\perp^2 v_z / 4\pi$). The dot-dashed line is the net energy flux due to sound waves ($\delta \rho \delta v_z c_s^2$; see the text). The dashed line is the term concerning the potential energy ($\rho v_z \Phi$). The circles are the ‘injection regions’ defined as the locations where the signs of $-B_z \delta v_\perp B_\perp / 4\pi$ change.

the midplane. This is a consequence of the breakup of channel flows, as described previously. Reconstructions break up channel flows and generate large amplitude ($|\delta B_{\perp}| > |B_z|$) Alfvén(ic) waves in both upward and downward directions. $\delta\rho\delta v_z c_s^2$ is also directed to the midplane, namely sound(-like) waves are generated by the reconstructions. The absolute value of the energy flux peaks at the injection regions at $z \approx \pm 1.6H_0$. The energy flux of sound waves to the midplane is larger than that of the Alfvén waves. On the other hand, the Alfvén wave component greatly dominates in the flux to the surfaces. This is because $\beta > 1$ (the gas pressure dominates) in $|z| \lesssim 2H_0$ and $\beta \lesssim 1$ near the surfaces.

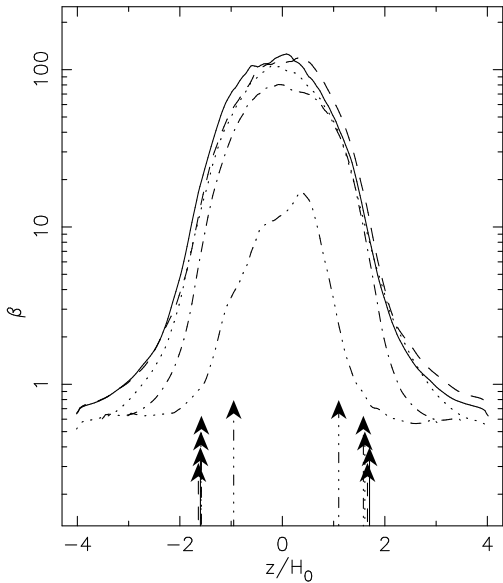


FIG. 4.— Dependence of the final β structure on initial magnetic fields. The dash-dot-dotted, dot-dashed, dotted, solid, and dashed lines correspond to the initial vertical fields with $\beta_0 = 10^4, 10^5, 10^6$, and 10^7 , and the initially toroidal field cases. The arrows indicate the locations of the injection regions defined as the points where the signs of $-B_z\delta v_{\perp}B_{\perp}$ change. Longer arrows correspond to smaller β_0 (the shortest arrows are for the initially toroidal case).

In order to study the effects of the initial magnetic fields, we performed the simulations with initial different vertical field strengths, $\beta_0 = 10^4, 10^5, 10^6, 10^7$, and initially toroidal field in $|z| < 3H_0$ with $\beta_0 = 10^6$ at the midplanes. Figure 4 compares $\langle\beta\rangle$ structures. Figure 5 compares the sum of disk mass fluxes from the upper and lower boundaries with various cases for the initial β_0 at the midplane. In all cases except the $\beta_0 = 10^4$ case, we averaged the variables during 200 rotations after the quasi-steady-states are achieved. For the $\beta_0 = 10^4$ case, we show the time averages during 25-55 rotations because the quasi-steady-state is not achieved but 90 % of the total mass escapes at 75 rotations as a result of the effective mass loss by disk winds.

All the cases of $\beta_0 \geq 10^5$ show very similar $\langle\beta\rangle$ structures (Figure 4): $\beta \approx 100$ at the midplanes, namely the magnetic energy can be amplified to $\approx 1\%$ of the gas energy. The β values decrease with increasing height mainly because of the decrease of the densities (the magnetic energies stay nearly constant; Figure 3). When the magnetic energy dominates ($\beta \lesssim 1$), the disk winds

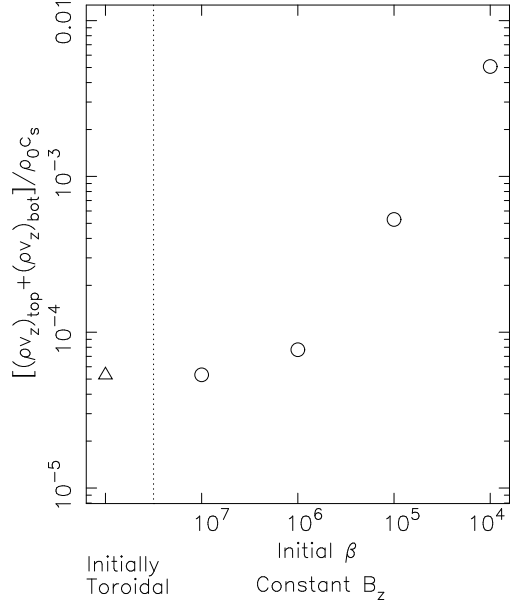


FIG. 5.— Sum of the mass fluxes normalized by $\rho_0 c_s$ of the disk winds from the top and bottom boundaries of the simulation box. The horizontal axis indicates the initial β_0 at the midplane for the vertical field cases circles. The initially toroidal case is plotted at the leftmost location (triangle).

start to accelerate. In the wind regions, the β values stay at $\beta = 0.1-1$, rather than further decrease, owing to the increased density by the lift-up gas in the winds. The locations of the injection regions also concentrate at $|z|/H_0 = 1.5-2$ except for the initial $\beta_0 = 10^4$ case. The plasma β values of the injection regions are 1-10; the magnetic energy is comparable to but slightly smaller than the equipartition value. This condition is favorable for driving mass motions by the breakup of large-scale channel flows; if the magnetic energy is larger, the field configuration becomes more coherent due to the tension so that reconnections hardly occur; if the magnetic energy is smaller, the reconnections cannot drive strong mass motion. The mass flux of the disk winds (Figure 5) only weakly depends on β_0 for $\beta_0 \geq 10^6$, while it increases for smaller β_0 almost in proportion with β_0 .

4. DISCUSSIONS

We have shown that the gas is lifted up from the injection regions at $|z|/H_0 \approx 1.5-2$ to the surfaces by the Poynting flux and streams out from the upper and lower boundaries of the simulation box. In effect, our results determine the condition of “mass loading” in various models of global disk wind (e.g., Blandford & Payne 1982; Kudoh & Shibata 1997, Ferreira et al 2006), in which one usually fixes the mass flux in advance by setting the densities at the ‘bases’ of winds. With our outgoing boundary condition, we implicitly assume that once the gas goes out of the z -boundaries of the simulation box it does not return. The validity of this treatment needs to be examined by the global modeling of accretion disks.

Although in the shearing box treatment the time-averaged net mass flow in the x -direction is zero, we can estimate the accretion velocity, $-v_r \approx \alpha c_s^2/r\Omega_0$, from the angular momentum balance under steady states, where r is a cylindrical distance from a central star

(Shakura & Sunyaev 1973). The ratio of the mass-loss rate, \dot{M}_z , from the simulation box by the disk winds to the mass accretion rate, \dot{M}_r , passing through the y - z plane becomes

$$\begin{aligned} \frac{\langle \dot{M}_z \rangle}{\langle \dot{M}_r \rangle} &\approx \frac{\int \int dx dy \langle \rho v_z \rangle}{\int dy \langle \Sigma \bar{\alpha} \rangle c_s^2 / (r \Omega_0)} = \frac{\langle \langle \rho v_z \rangle \rangle L_x r \Omega_0}{\langle \langle \Sigma \bar{\alpha} \rangle \rangle c_s^2} \\ &\approx 0.05 \left(\frac{r}{10 H_0} \right) \left(\frac{L_x}{H_0} \right), \end{aligned} \quad (4)$$

where $\Sigma = \int dz \rho$ and $\bar{\alpha} = \int dz \rho \alpha / \Sigma$; $\langle \rangle$ denotes the time-average and $\langle \langle \rangle \rangle$ is the average of time and x - y planes. The final value is estimated from $\langle \langle \rho v_z \rangle \rangle \approx 8 \times 10^{-5} \rho_0 c_s$ and $\bar{\alpha} \approx 0.012$ in our fiducial run for a moderately thin disk with $H_0/r = 0.1$. We should take the *above estimate as an upper limit* because the calculation with a larger vertical box size may give a smaller mass flux at the top and bottom boundaries. The angular momentum loss rates in vertical and radial directions give the same scaling,

$$\frac{\langle \dot{\mathcal{L}}_z \rangle}{\langle \dot{\mathcal{L}}_r \rangle} = \frac{\int \int dx dy \langle \rho v_z \rangle r^2 \Omega_0}{\int dy r \langle \Sigma \bar{\alpha} \rangle c_s^2} = \frac{\langle \langle \rho v_z \rangle \rangle L_x r \Omega_0}{\langle \langle \Sigma \bar{\alpha} \rangle \rangle c_s^2} \approx \frac{\langle \dot{M}_z \rangle}{\langle \dot{M}_r \rangle}, \quad (5)$$

because the time-averaged specific angular momentum carried by the winds is approximately the same as that in the disk material at the same radial position in the shearing box treatment. In a realistic situation, however, winds possibly carry a larger specific angular momentum than the disk material. For such studies, we need to model global accretion disks with disk winds, which is also important from the viewpoint of angular momentum evolution of the star-disk system (e.g. Matt & Pudritz 2005).

Hereafter we discuss the evolution of protoplanetary disks, as an application of our results. As a reference model, we use the minimum-mass solar nebula (MMSN) of Hayashi (1981), which gives the midplane density, $\rho_0 = 1.4 \times 10^{-9} (\frac{r}{1 \text{ AU}})^{-11/4} \text{ g cm}^{-3}$. Then, the initial vertical magnetic field of $\beta_0 = 10^6$ in our fiducial run corresponds to $B_{z,0} \approx 0.01 \text{ G}$, and the saturated field strength is $B \approx 1 \text{ G}$ at 1 AU.

First, we examine how much the disk wind contributes to the evaporation of protoplanetary disks (see e.g.

Dullemond et al. 2007, for other mechanisms). After the saturation of the magnetic fields, $\approx 5\%$ of the total disk mass is lost from the simulation box from 200 to 400 rotations by the disk winds in our fiducial case. Assuming a disk around a central star with the solar mass (1 rotation = 1 yr at 1 AU), we have the timescales of the evaporation, $\tau_{\text{ev}} \approx 4000 \text{ yr}$ at 1 AU, and $6 \times 10^5 \text{ yr}$ at 30 AU. Although this is rather short in comparison with recent observational results (typically $\tau_{\text{ev}} \sim 10^{6-7} \text{ yrs}$, e.g., Haisch, Lada, & Lada 2001), this is not a severe contradiction because we have not yet taken into account the global radial accretion of the disk mass, which continuously supplies the mass from the outer region. Another important issue that affects, and might reduce, the mass flux of disk winds is the effect of resistivity, which requires an additional detailed analysis of the ionization structure (Sano et al. 2000; Inutsuka & Sano 2005) and will be the scope of our next paper. Here, the estimated τ_{ev} should be taken as a lower limit.

The disk scale height has a relation of $H_0/r \propto r^{1/4}$ for the MMSN. Combining with Equation (4), we infer that the dynamical evaporation by disk winds, in comparison with accretion, becomes relatively more important in the inner parts of protoplanetary disks than in the outer regions for a constant initial β_0 structure ($B_{z,0}^2 \propto r^{-11/4}$ for the MMSN).

Finally, we should point out the effects of waves on dusts in protoplanetary disks. We have shown that the momentum flux of Alfvénic and sound-like waves directs to the midplane from the injection regions. The momentum flux of the sound-like waves ($\delta \rho \delta v_z$) can push dust grains to the midplane by gas-dust collisions. Dusts are usually weakly charged; in this case Alfvénic waves also contribute to the sedimentation of dusts to the midplane through ponderomotive force or dust-cyclotron resonance (Vidotto & Jatenco-Pereira 2006).

This work was supported in part by Grants-in-Aid for Scientific Research from the MEXT of Japan (T.K.S.: 19015004 and 20740100, S.I.: 15740118, 16077202, and 18540238), and Inamori Foundation (T.K.S.). Numerical computations were in part performed on Cray XT4 at Center for Computational Astrophysics, CfCA, of National Astronomical Observatory of Japan. The page charge of this paper is supported by CfCA.

REFERENCES

Balbus, S. A. & Hawley, J. F. 1991, ApJ, 376, 214
 Blandford, R. D. & Payne, D. G. 1982, MNRAS, 199, 883
 Brandenburg, A., Nordlund, Å., Stein, R., & Torkelsson, U. 1995, ApJ, 446, 741
 Clarke, D. A. 1996, ApJ, 457, 291
 Dullemond, C. P., Hollenbach, D., Kamp, I., & D'Alessio, P. 2007, Protostars & Planets V, B. Reipurth, D. Jewitt, and K. Keil, eds., Univ. of Arizona Press, 951, 555
 Ferreira, J., Dougados, C., & Cabrit, S. 2006, A&A, 453, 785
 Haisch, K. E. Jr., Lada, E. A., & Lada, C. A. 2001, ApJ, 553, 153
 Hawley, J. F., Gammie, C. F. & Balbus, S. A. 1995, ApJ, 440, 742
 Hayashi, C. 1981, Prog. Theoretical Phys. Supp., 70, 35
 Inutsuka, S. & Sano, T. 2005, ApJ, 628, L155
 Kudoh, T. & Shibata, K. 1997, ApJ, 474, 362
 Matt, S. & Pudritz, R. E. 2005, ApJ, 632, L135
 Miller, K. A. & Stone, J. M. 2000, ApJ, 534, 398
 Parker, E. N. 1966, ApJ, 145, 811
 Sakao, T. et al. 2007, Science, 318, 1585
 Sano, T., Miyama, S. M., Umebayashi, T., & Nakano, T. 2000, ApJ, 543, 486
 Sano, T. & Inutsuka, S. 2001, ApJ, 561, L179
 Sano, T., Inutsuka, S., Turner, N. J., & Stone, J. M. 2004, ApJ, 605, 321
 Shakura, N. I. & Sunyaev, R. A. 1973, A&A, 24, 337
 Stone, J. M., Hawley, J. F., Gammie, C. F., & Balbus, S. A. 1996, ApJ, 463, 656
 Suzuki, T. K. 2007, ApJ, 659, 1592
 Suzuki, T. K. & Inutsuka, S. 2005, ApJ, 632, L49 (SI05)
 —— 2006, J. Geophys. Res., 111, A6, A06101
 Thompson, K. W. 1987, J. Comp. Phys., 68, 1
 Tsuneta, S. et al. 2008, ApJ, in press (arXiv:0807.4631)
 Turner, N. J. & Sano, T. 2007, ApJ, 659, 729
 Vidotto, A. A. & Jatenco-Pereira, V. 2006, ApJ, 639, 416